AIAA Atmospheric Flight Mechanics (AFM) Conference
August 19-22, 2013, Boston, MA

AIAA 2013-4604

Mission Architecture Considerations for Recovery of High-Altitude Atmospheric Dust Samples

Matthew J. Miller,[1] Bradley A. Steinfeldt,[1] Robert D. Braun[2]
Georgia Institute of Technology, Atlanta, GA, 30332

In this investigation, a parametric study for the preliminary design of an Earth atmospheric dust collection and recovery mission has been conducted. The scientific goal of this mission is to sample and recover mesospheric dust and particulate matter. Suborbital flight trajectories, vehicle configurations, and deceleration technologies were analyzed using conceptual models. The trajectory is shown to be driven by the science objective (sample collection at 45 km to 85 km in altitude) and the target dust and particulate matter size. Preliminary vehicle configuration results indicate an insensitivty to landing dispersion and show a spacecraft-dependent relation to total heating. From the initial results, the design space is pruned and three reference mission architectures are defined—one which utilizes a standard disk-gap-band parachute and two that utilize supersonic inflatable aerodynamic decelerators. With use of the inflatable aerodynamic decelerator, drag modulation is shown to be able to reduce the landed uncertainty in downrange by approximately 6.8 km at the 95% confidence level.

Nomenclature

C_D	= coefficient of drag
C_{D0}	= DGB drag coefficient
C_X	= drag coefficient correction factor
k_s	= Sutton-Graves constant, kg$^{1/2}$ m$^{-1/2}$
M	= Mach number
n	= inflation power constant
q	= dynamic pressure, Pa
$\dot{q}_s$	= stagnation point heating rate, J/cm^2
r_n	= stagnation point radius, m
ρ	= sea level atmospheric density, kg/m^3
S_0	= reference area, m^2
t	= time, s
t_{SI}	= inflation start time, s
t_{FI}	= time at full inflation, s
v	= velocity, m/s

I. Introduction

The mesosphere which ranges in altitude from 45 km to 85 km has been a region of scientific interest for decades. Scientific estimates predict between 10 and 100 tons of meteoric material, micron to nanometer in size, enters the Earth's atmosphere per day.[1,2] These particles have been linked to polar summer mesospheric phenomena such as noctiluent clouds and polar mesosphere summer echoes.[3,4] Also known as meteoric smoke, mesospheric dust has been implicated in other atmospheric processes such as the production of nitric acid,[5] the removal of HNO_3 from the lower stratosphere, which alters ozone chemistry, and the condensation of sulphate aerosols in the stratosphere.[7] Various origins of the dust present in the mesosphere exist, including 2-5% of the matter which is estimated to have originated from intersteller space.[8,9] The composition and conditions of particle genesis of meteor smoke is highly sought after to further refine the scientific theories and models of the aforementioned atmospheric processes.[10]

---

[1] Graduate Research Assistant, Guggenheim School of Aerospace Engineering, AIAA Student Member

[2] David and Andrew Lewis Associate Professor of Space Technology, Guggenheim School of Aerospace Engineering, AIAA Fellow

Numerous attempts to capture mesospheric dust for laboratory analysis have been successfully demonstrated. Figure 1 shows historical sample collection campaigns, which began in the early 1960's. These early missions consisted of payload devices such as the Venus Flytrap,[11] Luster device,[12] and the ALARR device.[13] Each device, launched on a sounding rocket, was comprised primarily of contaminant-free flat plate sampling surfaces which were exposed perpendicular to the freestream between the altitudes shown in Figure 1. These devices were limited to capturing micron-sized particles and larger because submicron and nanometer scale particles tend to follow the flow around the payload thus not reaching the capturing surface.[14] In a continuing effort to examine the middle atmosphere, *in situ* particle measuring payloads were developed in the late 1980's and 1990's such as DROPPS, TURBO, MIDAS, Mini-MIDAS, and Mini-Dusty. More detailed information regarding *in situ* measure payloads and campaigns can be found in Refs. 15-18.

Within the last decade, there has been a renewed effort to capture mesospheric dust. The MAGIC (Mesospheric Aerosol – Genesis, Interaction and Composition) device was developed and flew its maiden flight early in 2005. This device, which has flown on all major mesospheric sounding rocket campaigns since 2005, specifically targets the nanometer scale meteoric particles that reside in the mesosphere. More detailed information regarding this payload device and its performance can be found in Refs.19- 21.

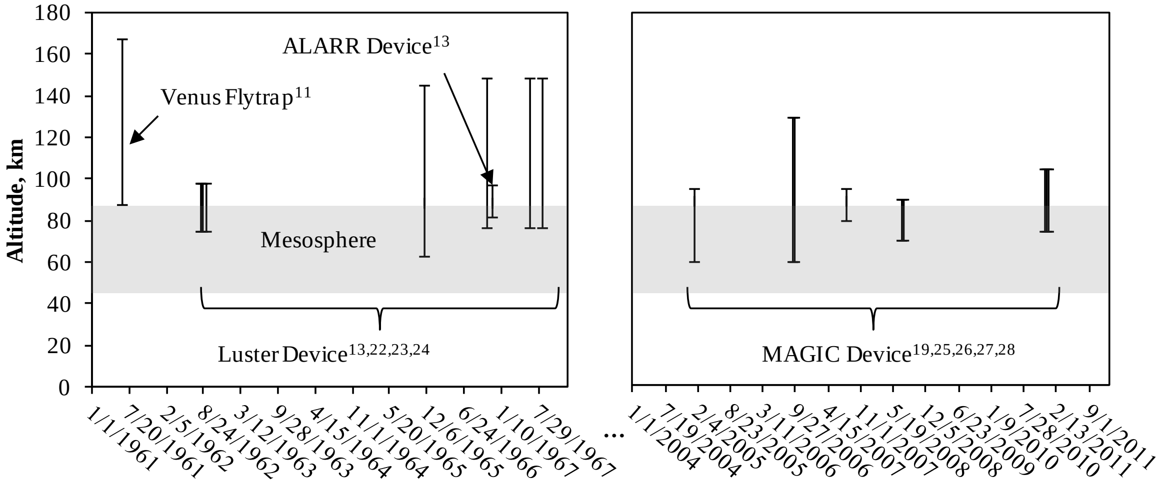

Figure 1. Altitude range for previous sample collection missions conducted on sounding rockets.

This study asseses a broad range of potential mission concepts and provides multiple reference architectures for mesospheric dust sample collection and retrieval, with an emphasis on precision recovery. Architecture trades span the launch vehicle, trajectory, sample collection system, bus geometry, and recovery system. The bus concept is formulated around three vehicle geometries including a standardized three-unit (3U) cubesat, a conventional sounding rocket payload, and a blunt body configuration. Supersonic aerodynamic decelerators and guided subsonic parachutes are considered as components of the recovery system. The effect of using drag modulation to control the downrange terminal state dispersion is investigated.

The analysis conducted in this study is broken into two phases: 1) an initial bounding analysis to characterize the tradespace, and 2) a more comprehensive end-to-end analysis to develop reference architectures. Utilizing a rapid conceptual design tool, the Planetary Entry Systems Synthesis Tool (PESST),[29] the bounding analysis systematically sweeps the design space to identify limiting cases. Physical constraints such as maximum altitude, sensed g's, and aerothermodynamic constraints are applied to the bounding analysis results to prune the design space for further investigation. The launch vehicle and ascent phase of mission architecture were included in the the end-to-end simulation. A Monte Carlo analysis was conducted in the end-to-end analysis framework to evaluate the precision capability of drag modulation using an inflatable aerodynamic decelerator as a means of drag modulation.

II. Mission Architecture

A. Requirements Definition

Table II below details the mission statement (MS) and primary mission objectives (PO) to be met by this mission.

Table II. Mission statement and mission objectives.

Statement ID	Description
MS-1	Provide a cost-effective and reliable method of acquiring samples of matter, including particles and dust, from Earth's mesosphere and returning them to Earth's surface

Objective ID	Description
PO-1	Obtain a scientifically significant sample of matter (particles and dust) from Earth's mesosphere (45 – 85 km) for analysis.
PO-2	Return the collected matter from Earth's mesosphere safely to the surface of Earth for recovery and analysis.

B. Design Space

There are several architectural trades associated with capturing dust particles in Earth's mesosphere and returning them to the surface. These trades are shown in Table III where items shown in grey are captured in the bounding analysis of this investigation and italicized items are traded in the end-to-end analysis. The maximum payload diameter of the available sounding rockets imposes a 16-inch maximum diameter constraint on the vehicle payload. This allows for direct integration of the sample collection device with the sounding rocket. For the delivery velocities, it is assumed the system will remain suborbital.

In this initial bounding analysis, four velocities were considered, 2 km/s through 5 km/s in increments of 1 km/s, with the upper velocity representing the maximum velocity the sounding rockets under examination (Improved Orion, Terrier-Improved Orion, and Terrier-Improved Malamute) can reasonably provide.[30] To assess the impact of vehicle configuration, three different outer mold lines (OMLs) for the vehicle's bus are considered. A 3U cubesat bus provides a commercial-off-the-shelf-option, whereas the cylinder is the more typical custom payload bus design for sounding rockets. A conventional shape for Earth entry systems, the 60^0 sphere cone, is also examined. In addition to vehicle shape, aerodynamic decelerators of varying types are examined across a wide range of conditions for improvements to the mission design.[31,32]

Table III. Mesospheric dust sample collection design space.

Configuration OML	3U Cubesat	60^0 Sphere Cone	Cylinder		
Delivery Velocity	2 km/s	3 km/s	4 km/s	5 km/s	
Delivery Altitude	<50 km	50-85 km	>85 km		
Sample Collection	*Before Decelerator Deployment*	*While Decelerator Deployed*			
Hypersonic Decelerator	Attached Rigid	Attached Inflatable	*Trailing Inflatable*	None	
Hypersonic Decelerator Deployment	*Immediate*	*Delayed*			
Supersonic Decelerator	Attached Rigid	Attached Inflatable	*Trailing Inflatable*	Parachute	None
Supersonic Decelerator Deployment	*Immediate*	*Delayed*			
Subsonic Decelerator	Attached Inflatable	Parachute	Same as Supersonic	None	
Subsonic Decelerator Deployment	*Immediate*	*Delayed*			
TerminalDescent	*Guided*	*Ballistic*			
Landing System	Impact	Air-Snatch			

Figure 2 shows a typical mission profile with alternative design options along a generic trajectory. Stage 1 consists of the launch of the sounding rocket. The payload and sounding rocket ascend along the trajectory during Stage 2. For scientific reasons, despinning of the payload is desired before sample collection. This is accomplished in Stage 3. Stage 4 consists of mesospheric dust sample collection, either with or without a deployable. Upon completion of the sample collection phase, payload recovery begins, either with or without a deployable decelerator. Stage 5 encompasses the terminal recovery stage. Depending on the needed landing precision, various options for terminal descent include continuing to utilize the deployable, an air-snatch system, a subsonic parafoil, or no system at all.

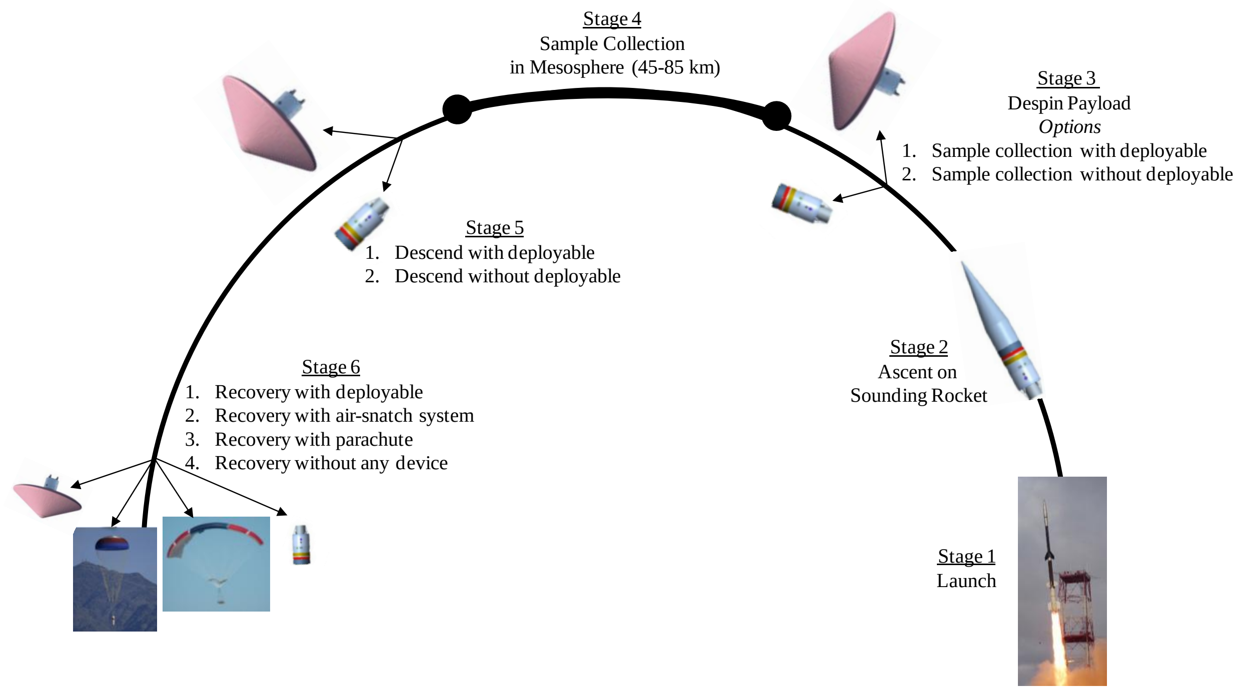

Figure 2. Mission architecture profile with alternative design options.

1. *Bus Configuration*

Three vehicle bus configurations were considered in the initial bounding analysis (Figure 3). The 3U cubesat was selected for its standardized bus structure with dimensions of 0.1 m x 0.1 m x 0.3 m. A 60^0 sphere cone configuration was also considered as a blunt configuration which has flight heritage at Earth (e.g., Stardust).[33] To maintain consistency with the cubesat, a reference area of 0.01 m^2 was enforced on the sphere cone. Typical payload configurations for the launch vehicles under consideration utilize a cylinder with a diameter of 0.356 m and a length of 1.22 m.

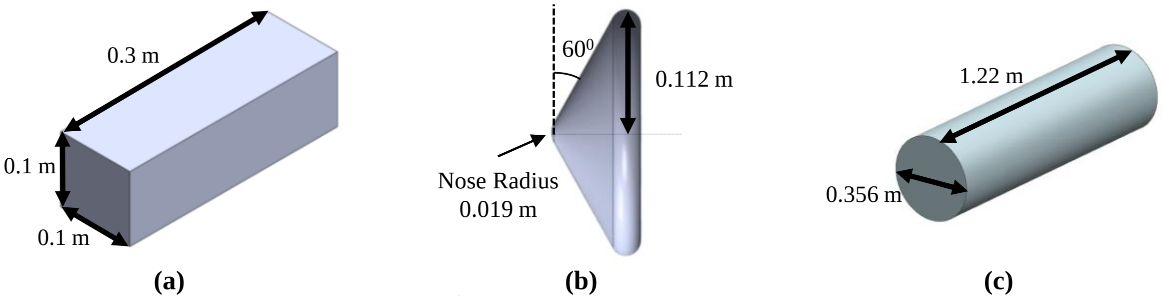

(a) **(b)** **(c)**

Figure 3. The (a) 3U Cubesat, (b) 60^0 Sphere Cone, and (c) Cylinder configurations considered.

The sample collection mechanism was assumed to be a container fitted with Aerogel pucks. Aerogel was proven as a viable medium for capturing high velocity particles in outer space on the Stardust mission[34] and could be implemented for sounding rocket particle capturing. The detailed design of the sample collection device is outside the scope of this study. For a generic sampling device, the Aerogel would be exposed to the freestream during the sample collection phase. After sample collection, the containment device would seal the Aerogel pucks, preventing the samples from being contaiminated during recovery. The bounding analysis does not examine the sample collection phase in detail, but the end-to-end analysis includes an analysis of the quantity of samples that can be collected.

2. *Decelerator System*

The three bus configurations shown in Figure 3 were combined with various deployable decelerators shown in Figure 4. Unique rigid deployables were examined for the cubesat and the cylinder. Using the aerodynamics modeling described in Section III.A., the drag coefficients were calculated for the rigid deployed cubesat and cylinder using referencs areas of 0.13 m^2 and 0.965 m^2, respectively, at zero angle of attack ($C_L = 0$ for all cases). Both of these deployable configurations provide the opportunity to implement unique decelerator technologies specific to their bus structures. Two other decelerators, a tension cone inflatable aerodynamic decelerator (IAD) and a parachute were also incorporated into the trade space.[32] The tension cone, sized from experimental wind tunnel testing articles used in Ref. 35, with a diameter of 0.6 m and 0.3 m were applied to the cubesat and sphere cone, respectively. Vehicle reference areas between the cubesat and the cylinder were used to scale the tension cone diameter for the cylinder to 0.9 m. The disk-gap-band (DGB) parachute was sized to 0.7 m in diameter for all three spacecraft configurations by using Viking-heritage vehicle-diameter to parachute-diameter ratios.[36] Use of a precision-guided lifting parachute was also considered to reduce landing dispersions.

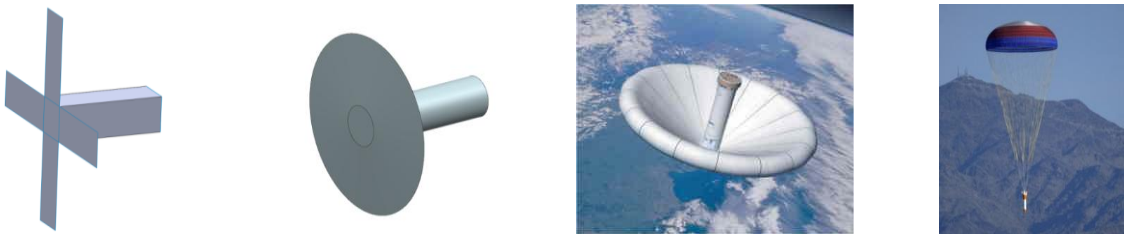
(a) **(b)** **(c)** **(d)**

Figure 4. Deployable decelerator considerations which includes (a) Rigid Deployable for Cubesat, (b) Rigid Deployable for Cylinder, (c) Tension Cone IAD, and (d) Disk-Gap-Band Parachute.

III. Modeling

For the bounding analysis, trade studies for each candidate architecture were performed via numerical simulation using conceptual design tools integrated within a multidisciplinary design framework using PESST, a conceptual design tool for entry systems.[29] The components of this framework allow for integrated analysis of system aerodynamics, the trajectory, and the heating characteristics. In addition, analysis of the decelerator system and subsonic parachute is enabled by this framework. This multidisciplinary environment enables simultaneous evaluation of the candidate architecture's performance in terms of mass at both the system and component level as well as trajectory dependent characteristics (e.g., landing accuracy and heating).

An event-based simulation including the launch phase was used in the end-to-end analysis. Primary inputs to this simulation environment include aerodynamic databases, launch vehicle performance, payload mass, deployable decelerator type and deployment conditions. This higher-fidelity analysis allows time dependent output including sampling time, trajectory range, sample mass flow, number of particles (based on dust particle profiles published by Hunten, et al.)[37], dynamic pressure, heating, and state data (e.g., altitude and velocity).

A. Aerodynamics

1. Bus Aerodynamics

For the bounding analysis, Modified Newtonain aerodynamics was utilized to estimate hypersonic aerodynamics.[31] Results were generated with a first-order industry standard tool, the configuration based aerodynamics (CBAERO) tool.[39] In this conceptual study, the center-of-gravity is modeled along the axis of symmetry such that the vehicle trims at a 0° angle of attack. Table IV summarizes the vehicle aerodynamics used in the bounding analysis. The end-to-end analysis incorporated more detailed drag coefficients as a function of Mach number. The drag coefficient values as a function of Mach number for the bulbous sounding rocket payload fairing was estimated to be similar to that of the 5.56mm BRL-1 ballistic projectile[40] and reference literature was used for the cylindrical bus structure.[41] Figure 6 below shows their respective drag profiles where the reference areas used were 0.1276 and 0.099 m^2, respectively.

Table IV. Bounding analysis vehicle aerodynamics.

Vehicle	Reference Area (m^2)	Coefficient of Drag (C_D)
3U Cubesat	0.010	1.988
60^0 Sphere Cone	0.010	1.564
Cylinder	0.025	1.988

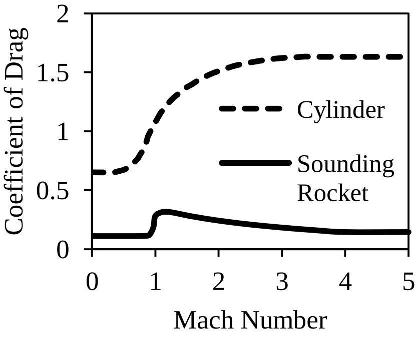

Figure 6. Mach dependent aerodynamics for the sounding rocket and cylindrical bus structure.[40,41]

2. *Decelerator Aerodynamics*

The various decelerators and their respective aerodynamic input parameters are summarized in Table V. Mach dependent aerodynamic data, as shown in Figure 7, was used.

Table V. Decelerator aerodynamics parameters.

Decelerator	Input Parameters	
	Diameter (m)	*Reference Area (m^2)*
Rigid Deployable (Cubesat)	0.70	0.13
Rigid Deployable (Cylinder)	0.63	0.97
Disk-Gap-Band Parachute	0.70	0.13
Stock DGP Parachute	8.5	56.7
Tension Cone		
Cubesat	0.30	0.07
Cubesat	0.60	0.28
Cylinder	0.90	0.64

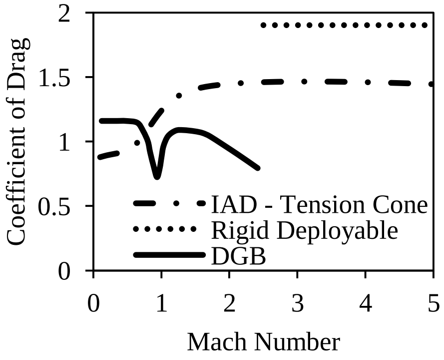

Figure 7. Mach dependent aerodynamics for deployables.

B. Trajectory

A three degree-of-freedom simulation was used to determine the trajectory. For the bounding analysis, a fixed-step, 4th-order Runge-Kutta algorithm was used with 0.1 s time steps while for the end-to-end analysis an adaptive-step integration scheme was used. For the bounding analysis, a set of planet-relative initial conditions corresponding the beginning of the sample collection phase were propagated until the terminal altitude condition is achieved (either a maximum altitude or minimum altitude). For the end-to-end analysis, the initial state corresponded to that on the launch pad at White Sands Missile Range.

C. Thermal Response

For the bounding analysis, the Sutton-Graves approximation, as shown in Equation 1 for the stagnation point convective heating was used.[42]

$$\dot{q}_s = k_s \sqrt{\frac{\rho}{r_n}} \mathrm{v}^3 \tag{1}$$

Since the sphere cone flies at 0° angle-of-attack, the stagnation point is taken to be the nose radius of vehicle such that r_n = 0.0188 m and the nominal value of the Sutton-Graves constant, k_s , is 1.74153×10^{-4} $kg^{1/2}$ $m^{-1/2}$. As the cubesat and cylinder vehicles have a flat frontal area, an approximation of the effective stagnation point radius is derived by dividing their respective reference area by two. Table VI summarizes the reference areas and stagnation points used in this analysis for each vehicle.

Table VI. Vehicle stagnation radius values.

Vehicle Bus	Stagnation Radius (m)
3U Cubesat	0.0500
60^0 Sphere Cone	0.0188
14” Diameter Cylinder	0.1778

For the end-to-end analysis, regime-dependent heating was determined using CBAERO for each of the vehicle bus configurations as a function of Mach and dynamic pressure.

D. Drag Modulation

Drag modulation is a drag-only control mechanism which employs a discrete event to alter the drag area of a vehicle. In this study, we refer to this discrete event as the deployment of an inflatable aerodynamic decelerator to control vehicle downrange and dynamic pressure for parafoil deployment. For a more detailed discussion on drag modulation, refer to Refs. 43-44. Figure 8 below shows the notional drag modulation trajectory profile incorporated into the end-to-end analysis for this study.

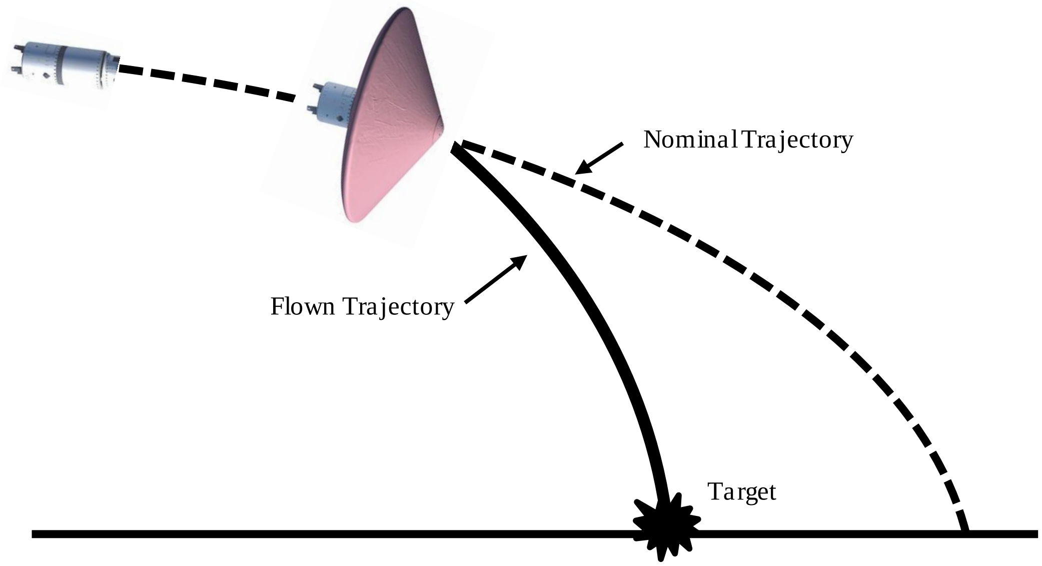

Figure 8. Drag modulation trajectory profile.

E. Analyses

1. Bounding Analysis

The initial altitude in the bounding analysis was varied between 45 km and 85 km, which corresponds to the altitude regime of the mesosphere. The flight-path angles at the initial state were varied between 0^0 and 15^0. All other variable ranges are illustrated in Table VIII. If modeled in an architecture, the deployable decelerators were initiated at or below Mach 3. Due to packing contraints on the the 3U cubesat, a maximum payload mass constraint of 10 kg was applied to each vehicle. To account for uncertainty in atmospheric and vehicle drag, off nominal cases were also examined. By incorporating these uncertainities, landing dispersions were examined for each case.

Table VIII. Bounding analysis parameter sweep.

Parameters	**Variable Sweep**				
Vehicle	3U Cubesat	60^0 Sphere Cone	Cylinder		
Altitude, km	45	65	85		
Velocity, km/s	2	3	4	5	
Flight Path Angle,Deg	0	7.5	15		
Decelerator Type	None	DGB Parachute	Tension Cone IAD	Deployed Cubesat	Deployed Cylinder
IAD Diameter, m	Cubesat = 0.6 m	Cubesat = 0.3 m	Cylinder = 0.9 m		
DGB Diameter, m	0.7				
Decelerator Deployment Conditions	DGB (M=1) IAD (M=2) DC* (M=1) DCy** (M=1)	DGB (M=2) IAD (M=3) DC (M=2) DCy (M=2)	DC (M=3) DCy (M=3)		
Entry Mass, kg	10				
Vehicle C_D	Nominal	-15% Nominal	+15% Nominal		
Atmospheric Density	Nominal	-25% Nominal	+25% Nominal		

*DC = Rigid Deployed Cubesat **DCy = Rigid Deployed Cylinder

2. *End-to-End Analysis*

The end-to-end analysis investigated system level trade studies and multiple architectures varying in capability and complexity. Three deployable recovery devices were examined using the simulation. These devices included a stock sounding rocket DGB parachute, a tension cone inflatable aerodynamic decelerator, and a precision guided parachute. These devices' performance characteristics and required deployment conditions were evaluated in the mission profile for the optimized trajectorys explained below.

The optimization problem for this mission is given by

Maximize: $\mathcal{J} = \alpha N_{particles} + \beta t_{meso} + \gamma d_{meso} + \delta m_{meso}$

By varying: Launch elevation ($77^0 \le \lambda \le 85^0$)

The results presented in this study are from the single objective optimization analyses. The trajectory profile of the mission was optimized by varying launch elevation angle and vehicle payload mass to find each of the following:

A) maximum number of particles captured in mesosphere ($\alpha = 1$, $\beta = 0$, $\gamma = 0$, $\delta = 0$)
B) maximum time in the mesosphere ($\alpha = 0$, $\beta = 1$, $\gamma = 0$, $\delta = 0$)
C) maximum range in the mesosphere ($\alpha = 0$, $\beta = 0$, $\gamma = 1$, $\delta = 0$)
D) maximum collected sample mass ($\alpha = 0$, $\beta = 0$, $\gamma = 0$, $\delta = 1$)

The number of a given size of particle at a given altitude is estimated by the profiles given by Hunten in Ref. 37.

Deployable devices were not implemented in the optimization of the trajectories since the objective functions were concerned with only mesospheric sampling. The optimized trajectory to maximize the capture of 1 nm particles was selected for further analysis with deployable devices. Drag modulation performance was also evaluated for this optimized trajectory.

A sweep of aforementioned launch elevation angles and payload masses was also conducted to address the limitations of the Improved-Orion launch vehicle. Analysis of the launch sequence events was conducted to evaluate impact on the trajectory decelerator phase. This includes impacts on downrange, deployment dynamic pressure and deployment mach environments for deployables.

For this analysis, a stock high altitude sounding rocket DGB was deployed at 73 km altitude with 25 seconds of inflation time.[45] The DGB parachute has extensive flight demonstration and performance capability.[46] Parachute inflation loads were estimated using the opening loads equation shown in Equation 2 where q is the dynamic pressure of the freestream, C_{D0}, is the drag coefficient of the DGB parachute, S_0 is the reference drag area of the DGB parachute, C_X is a drag coefficient correction factor, 1.45, t, is the time step of the solver, t_{SI} is the time at start of inflation, t_{FI} is the time at full inflation, and n is a power constant assumed to be 2 for this analysis.[36]

$$F_p = q C_{D0} S_0 C_X \left(\frac{t - t_{SI}}{t_{FI} - t_{SI}}\right)^n \tag{2}$$

The stock sounding rocket 8.5 m DGB upper mass limit of 24 kg as well as the cylindrical bus configuration was implemented in this study as the baseline vehicle configuration.[30] A 0.9 m tension cone IAD was also implemented in this analysis as the supersonic decelerator. The guided parachute deployment constaints were taken into account even though this phase was not simulated.[47,48] Deployment constraints are summarized in Table IX for all deployables.

Table IX. Deployment constraints for deployable devices.

Deployable Type	Deployment Conditions	
	Mach Number	*Dynamic Pressure (kPa)*
DGB	1.0 - 2.5	$4\text{x}10^{-5}$ - 0.9
IAD	1.0 - 4.0	$1\text{x}10^{-3}$ - 25
Guided Parafoil	0.01 - 0.12	$4\text{x}10^{-5}$ - 1.2

a. *Monte Carlo Parameters*

To investigate the overall performance improvement of drag modulation implementation, a Monte Carlo analysis of five hundred runs was conducted. Table VII shows the parameters which were varied along with their nominal value, distribution type, and deviation value. Figure 9 below shows the atmospheric density, Eastward and Northward wind variation as a function of altitude for the nominal launch site at White Sands. Earth-GRAM 2007 was used to generate all atmospheric information, including standard deviations as a function of altitude.[49]

Table VII. Vehicle and state parameters.[50]

Parameter	Nominal Value	Distribution Type	Deviation (3-sigma or min/max)
Launch Elevation Angle, Deg	81.0	Uniform	+/- 0.1
Launch Azimuth Angle, Deg	355.0	Uniform	+/- 0.1
Payload Mass, kg	24.0	Uniform	+/- 0.5
Mass-drop Time, s	10.0	Uniform	+/- 1.0
Thrust Multiplier (Booster)	1.0157	Gaussian	0.03
Thrust Multiplier (Sustainer)	1.0157	Gaussian	0.03
Drag Coefficient Multiplier (Sounding Rocket)	1.0	Gaussian	0.3
Drag Coefficient Multiplier (Payload Bus)	1.0	Gaussian	0.3
Drag Coefficient Multiplier (Decelerator)	1.0	Gaussian	0.3

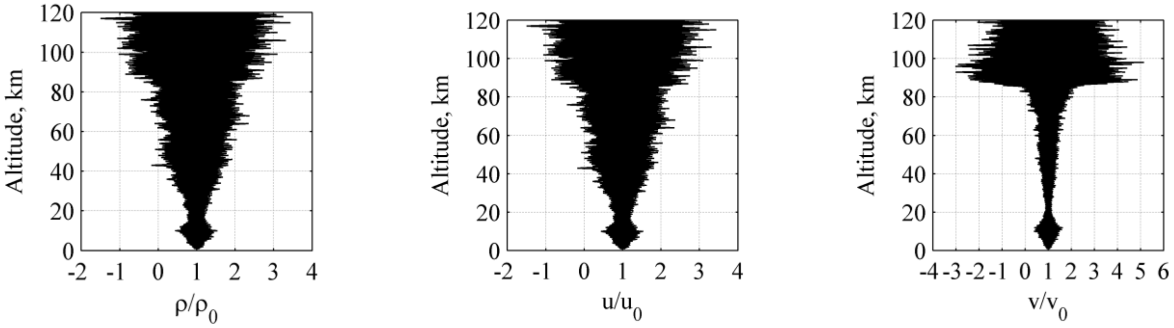

(a) **(b)** **(c)**

Figure 9. Atmosphere variation as a function of altitude for (a) density, (b) East winds, and (c) North winds.

IV. Results and Discussion

A. Bounding Analysis Results

Several practical design constraints exist in this design space. These include:

1. A limitation on the maximum altitude of the sample collection vehicle: $h_{\max} < 130$ km
2. A limitation on the maximum sensed g-load: sensed g < 30 g's

These constraints were used in the bounding analysis to prune the design space results by a factor of two. Bounding analysis results focused on the maximum heat rate experienced throughout the flight regime, the maximum sensed g-force experienced during flight, and the landing dispersions generated from variations in vehicle drag coefficients and atmospheric density.

Vehicle peak heat rate values steadily increase as initial velocity increases. For all four velocity cases, the sphere cone experiences overall higher heat rates. Previous Earth sample return missions such as Stardust and Genesis experienced estimated heat rate peaks on the order of 1200 W/cm^2 and 700 W/cm^2, respectively.[51] Configurations at all initial velocity states experience heating rates less than historical precedent. However, the configurations with velocities less than 3 km/s would require less thermal protection mass due to their decreased experienced peak heat rates, making these cases a more favorable option.

Peak g-loading values depicted an even distribution among the candidate bus configurations. A maximum limit of 30 g's was imposed on the final data set to minimize the structural mass requirements of the bus structure. Variation in vehicle drag coefficient and atmospheric density were used to generate the final landing dispersions. A majority of configurations yield landing dispersions less than 40 km, with the more variable landing dispersions occurring with the high velocity cases with medium flight path angles. Landing dispersion trends were shown to be independent of vehicle configuration. Figure 10 shows the bounding analysis results for the 2 km/s initial velocity cases.

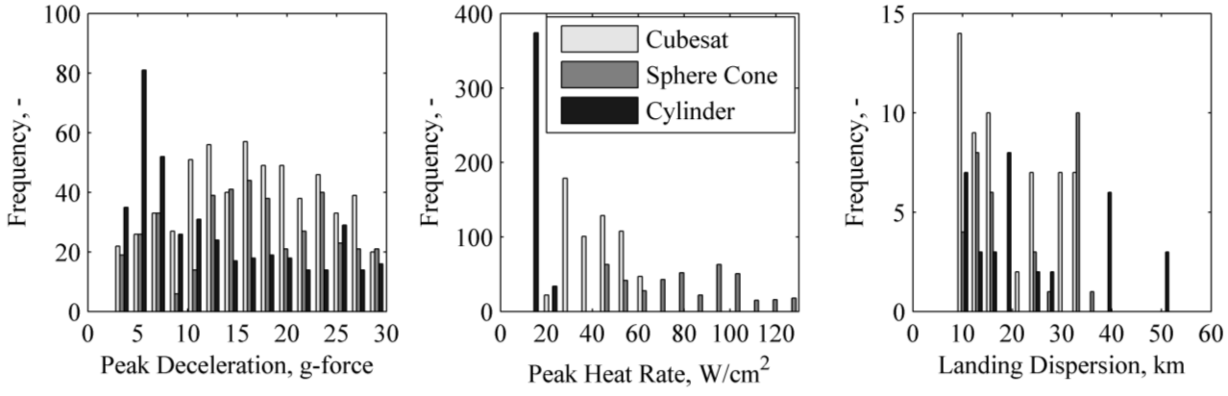

(a) **(b)** **(c)**

Figure 10. Bounding analysis distributions for (a) peak deceleration, (b) peak heat rate, and (c) downrange landing dispersion for 2 km/s initial velocity cases.

Due to the heating and g constraints, the results of the bounding anlaysis allowed the end-to-end analysis to focus on slower velocity archtiectures with supersonic deceleration devices (as opposed to the hypersonic decelerators) excluding the sphere-cone. The complexity as well as additional g-loading and heating of the rigid decelerator configurations allowed them to be excluded from further consideration. Finally, it is noted that to enable precision delivery of the payload, a low flight path angle or a high flight path angle during sample collection is desirable.

B. End-to-End Analysis Results

The results of the bounding analysis indicated a more detailed focus on initial velocity states less than 2 km/s flown at high launch angles to minimize heating rate and landing dispersions. Much of the velocity space examined in the bounding analysis also revealed that most of the sounding rocket vehicles offered launch capabilities far in exceess of what was needed to reach the top of the mesosphere.

1. Trajectory Optimization

Several practical design constraints exist in this design space in addition to the constraints suggested by the bounding analysis. Single objective optimizations were peformed using a gradient based algorithm using the following objective function formulation where λ is the launch elevation angle. Launch elevation angle was bounded by the Improved-Orion launch vehicle.[30]

Optimized trajectories for the cylinderical spacecraft configuration are shown in Figure 11. The cylindrical bus was used because this structure offers the least complex integration option between sounding rocket and the vehicle bus. The trajectories are broken into specific phases. The sounding rocket provides thrust during the boost phase in a two segment (booster and sustainer) burn with final burnout occurring at 27 seconds after ignition. The payload and sounding rocket structure then enters a coast phase for a specified amount of time. The structural mass of the sounding rocket, approximately 110 kg, is then ejected and the vehicle bus enters a short duration despin phase (not modeled in this study) to prepare for sample collection. Sample collection occurs while the vehicle is above 45 km. The vehicle enters another coast phase once sample collection is complete. As the objectives are independent of the deceleration technology, decelerators are not incorporated into these optimized trajectories, but are examined in Section IV.B.3.

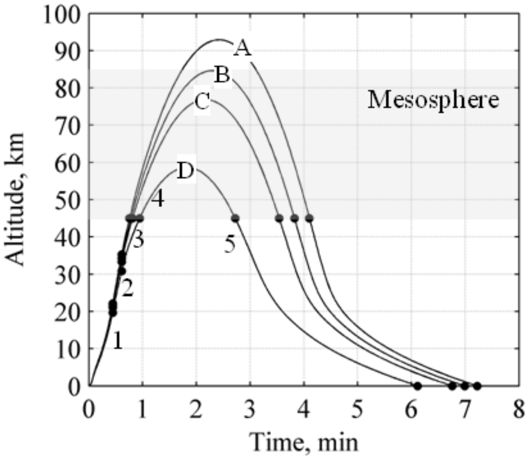

Phase	Description
1	Boost Phase
2	Coast Phase
3	Despin Phase
4	Sample Collection Phase
5	Descent & Recovery Phase

	Function Objective			
	Maximum number of 1 nm particles captured	Maximum time in the mesosphere	Maximum range in the mesosphere	Maximum collected sample mass
Trajectory	A	B	C	D
Launch Elevation Angle, Deg	82.5	80.9	79.9	77.0

Figure 11. Optimized trajectories.

The optimization analysis results indicated a sample collection efficient trajecotory with a payload mass of 24 kg and launch elevation angle of 81 degrees. This trajectory provides a compromise between each of the objectives except for the sample mass and is used as the reference trajectory for the remainder of this study.

2. *Launch Sequence Evaluation*

A key aspect of the trajectory optimization is sequencing of events during launch. These events have a large impact on later stages in the trajectory including the decelerator deployment environment and downrange capability. The sounding rocket structure mass drop occurs between rocket burnout at 27 s after ignition and start of sample collection at 45 km. On average, the time gap between these two stages is on the order of 20-30 s. A mass drop sequence occurring at 10 seconds post engine burnout was used for all trajectories presented in this study to ensure the vehicle would reach the mesosphere for all anticipated mass and launch elevation angle combinations.

3. *Drag Modulation Evaluation*

For a nominal atmospheric and drag coefficient trajectory with deployment of a tension cone at 45 km altitude, a maximum of 10.25 km reduction is achieved for the lowest launch elevation angle relative to the no deployed decelerator trajectory. The earlier the decelerator is deployed during the trajectory, the more effective the drag modulation becomes. When incorporating the drag modulation deployment algorithm, it is assumed that the deployable can activate after apogee while still in the sample collection phase of flight. Sample collection continues until 45 km altitude is reached during descent, then the deployable is eligible to activate. Figure 12 shows how the downrange reduction for a sweep of trajectories with changes in launch elevation angle and vehicle bus mass. The aforementioned optimized trajectory has a reasonably high launch angle (81°) which reduces overall drag modulation capability. However, higher launch elevation trajectories lead to steeper flight path angles during sample collection, which the bounding analysis showed to reduce the landing dispersion. For a given launch elevation angle, lower mass payloads exhibited decreasead drag modulated downrange performance diminished differences in the ballistic coefficient.

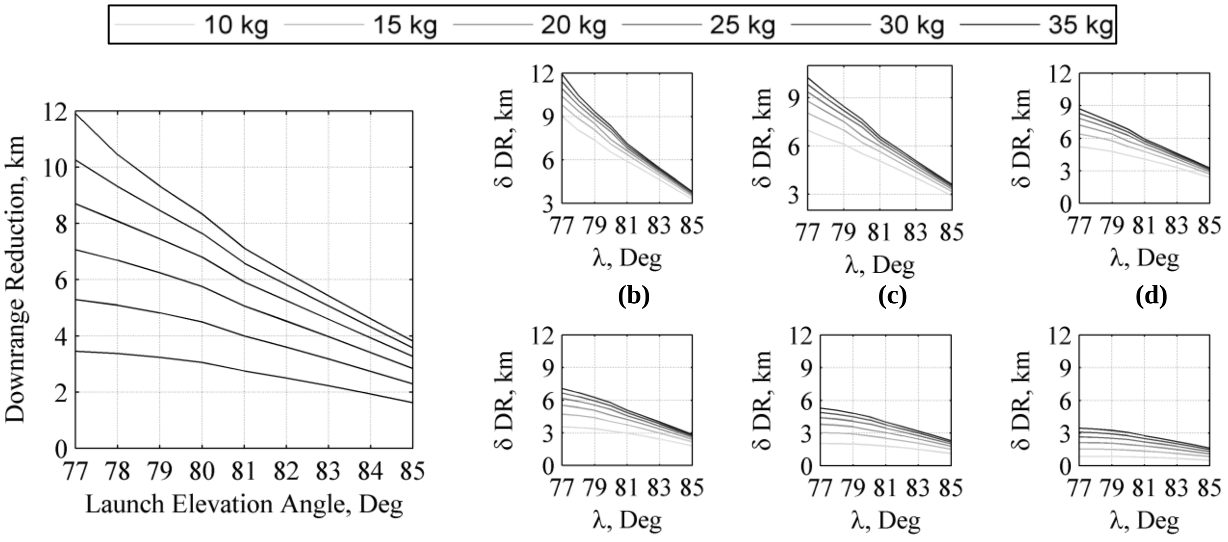

(a) (e) (f) (g)

Figure 12. Downrange reduction using a 0.9 m diameter tension cone deployed at (a) altitudes between 25 and 50 km for a 35 kg mass payload; for payload masses ranging from 10 to 35 kg with deployment occurring at (b) 50 km , (c) 45 km, (d) 40 km, (e) 35km , (f) 30 km, (g) 25 km.

As shown in Figure 13, the deployment conditions of the IAD over the same swep of trajectories do appear favorable. The Mach number and dynamic pressures at deployment altitudes between 25 km and 50 km for a variety of payload masses and launch elevation angles all meet the deployment constraints of the IAD. The ballistic portion of the trajectory for a vehicle bus with a payload mass less than 20 kg becomes dominated by the aerodynamic drag. As a result, less severe deployment environments over the range of deployment altitudes examined are experienced for lower mass systems.

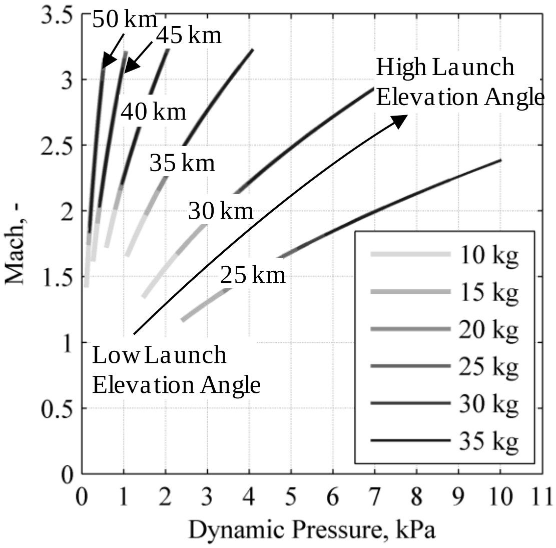

Figure 13. Mach vs dynamic pressure at deployment altitudes of 25 to 50 km of a 0.9 m IAD as a function of launch elevation angle between 77^0 and 85^0 and payload masses between 10 and 35 kg.

Figure 14 shows the Mach and dynamic pressure conditions at 6 km altitude for when both an IAD is used and is not used. Parafoil deployment when an IAD is deployed at 45 km achieves the required deployment constraints. However, if no IAD is deployed during in the trajectory, only small mass payloads are likely to meeting the parafoil deployment constraints. For a given payload mass, the parafoil deployment environment at 6 km is insentive to launch elevation angle when an IAD is deployed during the trajectory.

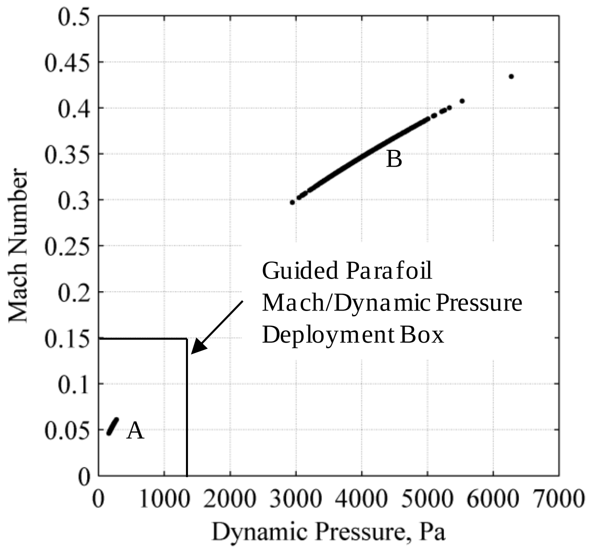

Figure 14. Mach vs dynamic pressure parafoil deployment dispersions at 6 km altitude (A) with and (B) without IAD deployment at 45 km altitude.

The Monte Carlo downrange and crossrange results for an DGB decelerator deployed at 73 km, a 0.9 m IAD deployed at 45 km, and a 0.9 m IAD deployed using the drag modulation algorithm are shown in Table VIII and Figure 15. As shown in Fig. 15, at the 95% confidence level, the DGB's landed footprint is 66.8 x 30.4 km, the IAD's footprint is 65.6 x 4.6 km and with the addition of drag modulation, the IAD achieves a 58.8 x 3.8 km footprint. Incorporation of drag modulation reduces delivery footprint in major-axis by approximately 6.8 km (at the 95% C.I.) through significant clustering of points with downrange distances that match the target. The crossrange errors associated with the DGB are appreciably larger due to being exposed to wind variations during the relatively lengthy descent (>1 hour) and decrease with the later deployment of the IAD.

Table VIII. Landing statistics.

Architecture	Mean Error in Downrange, km	Downrange Error Standard Deviation, km	Mean Error in Crossrange, km	Crossrange Error Standard Deviation , km
DGB	10.88	13.66	5.00	6.24
IAD	10.62	13.40	0.74	0.94
IAD with Drag Modulation	9.25	12.02	0.62	0.78

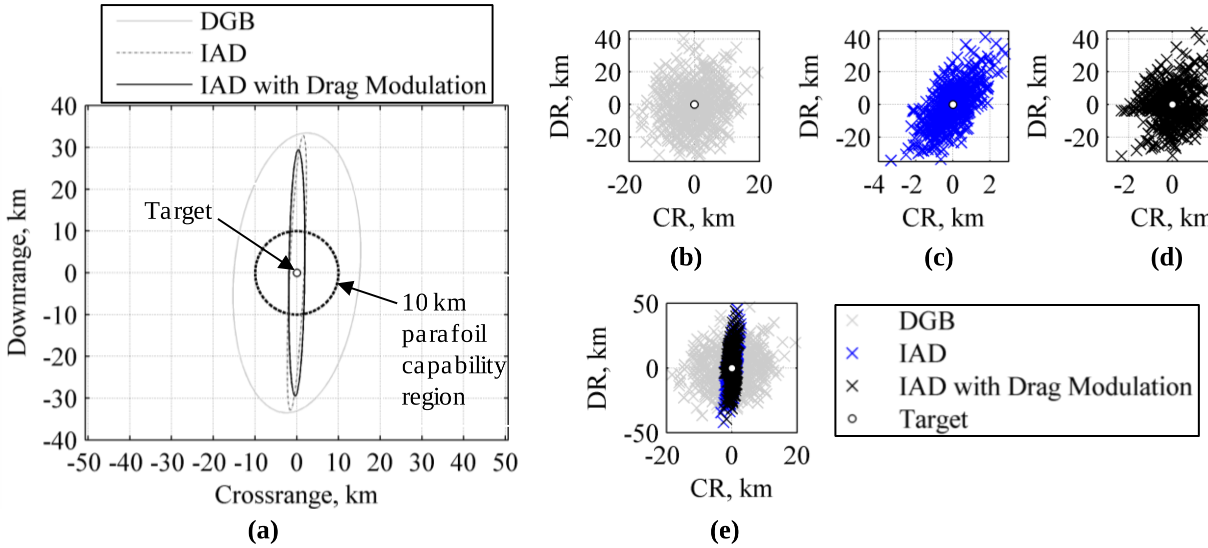

(a) (b) (c) (d) (e)

Figure 15. Downrange & crossrange dispersions (a) footprint at 95% confidence interval, (b) 8.5 m DGB deployed at 73 km, (c) 0.9 m IAD deployed at 45 km, (d) 0.9 m IAD deployed using drag modulation, (e) combined results.

C. Reference Architectures

Three candidate reference architectures were formulated for further examination. These architectures provide varied levels of technology readiness, complexity and performance and are shown in Figure 16. A detailed description of each architecture is presented in the following subsections.

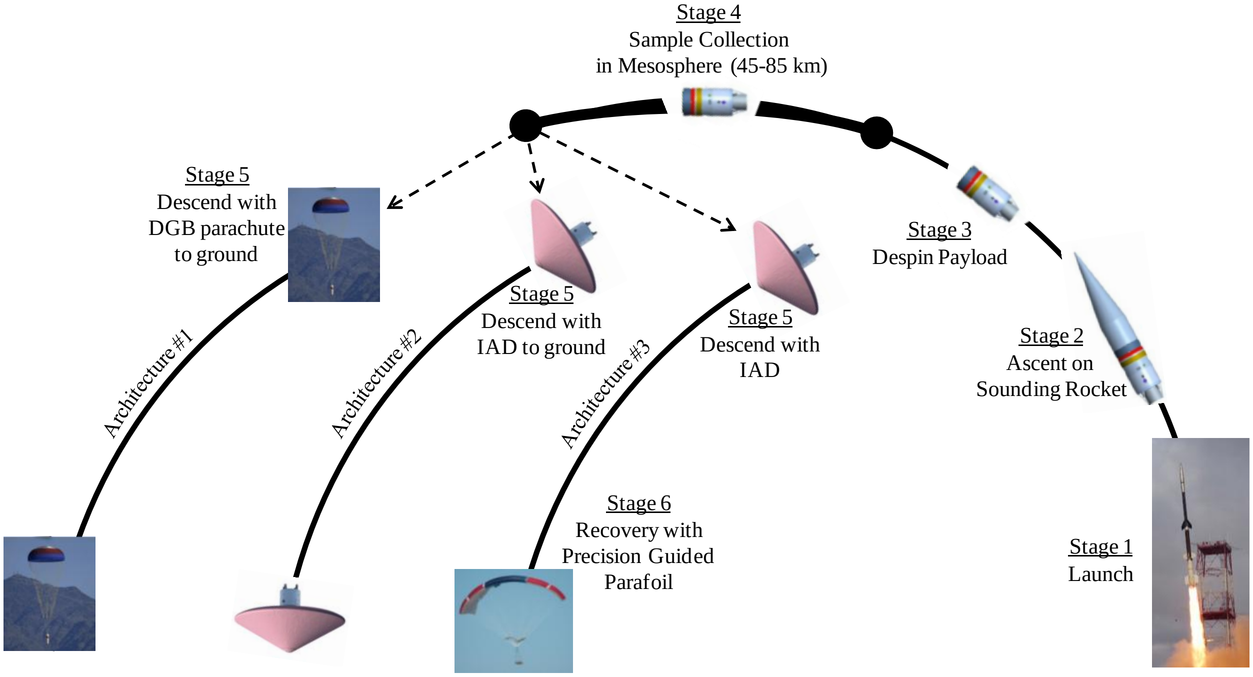

Figure 16. Concept of operations for three reference architectures and their stages from launch to landing.

1. Architecture #1: Stock Sounding Rocket DGB

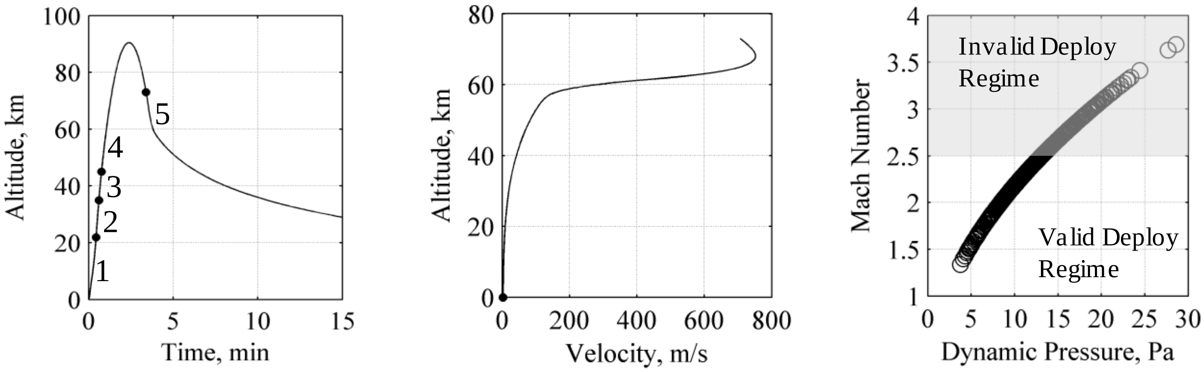

(a) **(b)** **(c)**

Figure 17. Architecture #1 trajectory details showing altitude as a function of (a) time during launch to DGB deployment, (b) time from launch to landing, (c) DGB deployment condition dispersion results.

Architecture #1, as shown in Figure 17, represents a mesospheric sample collection platform which utilizes stock sounding rocket decelerator hardware. The maximum payload capability of the 8.5 m DGB is 24 kg. The total flight duration for this architecture is approximately 2 hours. Even though this recovery system is a standard option, this flight time is lengthy and could pose challenges for designing the sample containment device. The DGB parachute must also be deployed at sufficiently high altitudes so as not to exceed the specified dynamic pressure, and Mach number limits. Sample collection duration is impeded due to having to be deployed within the mesosphere and will yield approximately 20% fewer number of captured mesospheric samples. Downrange control is not a realistic option for this recovery configuration. Once deployed, the system remains aloft in the atmosphere for an extended period of time, making it susceptible to drifting in the wind.

2. *Architecture #2: Supersonic IAD*

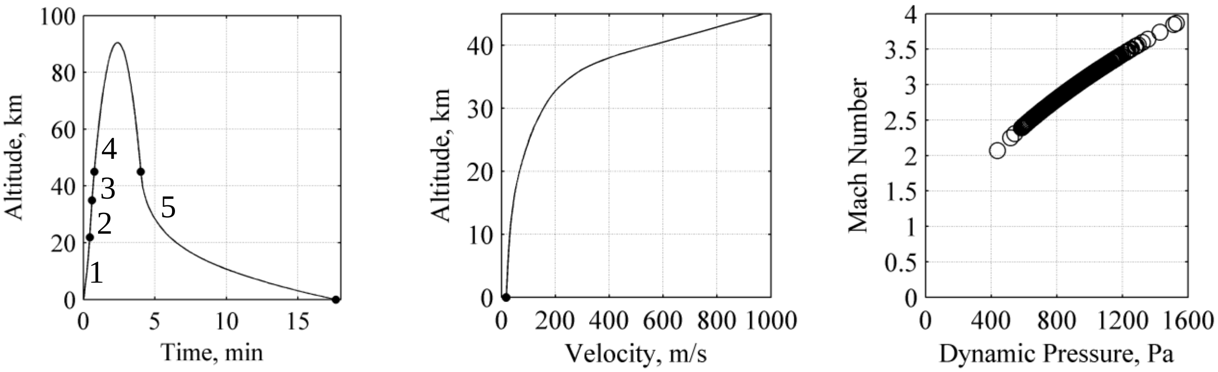

(a) **(b)** **(c)**

Figure 18. Architecture #2 trajectory details showing (a) launch to landing, (b) from IAD deployment to landing, and (c) IAD deployment condition at 45 km dispersion results.

Architecture #2, as shown in Figure 18, represents a mesospheric sample collection platform which utilizes a supersonic IAD. This device is capable of deploying in flow environments up to Mach 4 and 25 kPa dynamic pressure.[31] For the trajectories seen in this analysis, the end of the sample collection phase environment is suitable for IAD utilization. Using the compromised science objective trajectory, the total flight duration for this architecture is 15 minutes. The IAD may also be triggered to deploy at alternate altitudes to 45 km which will alter the landed downrange of the vehicle. The sample collection phase can be completed in its entirety within the mesosphere before the decelerator phase is activated which maximizes the potential to capture mesospheric particles. Control of downrange dispersions is determined by the initial launch elevation angle, which can be reduced by up to 11 km for large elevation angles. This architecture expands IAD technology as IADs of this size, to date, have not flown in these environments.

3. *Architecture #3: Supersonic IAD with Precision Guided Parafoil*

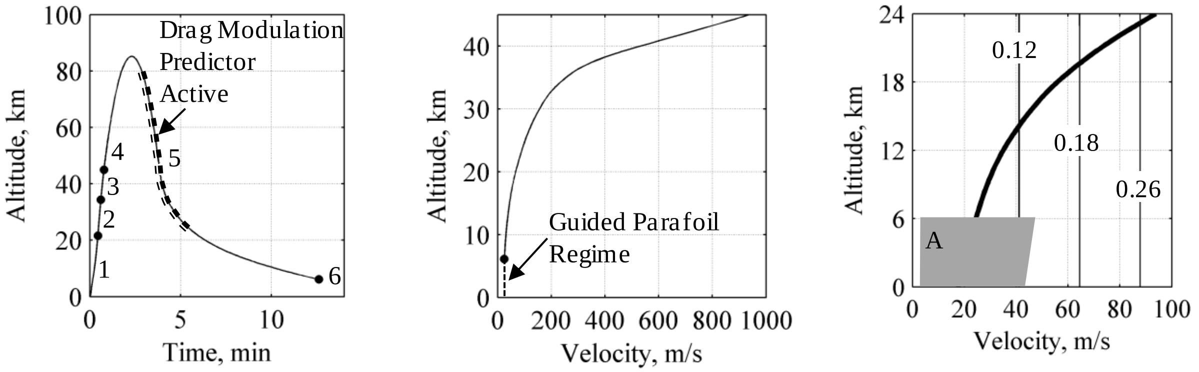

(a) **(b)** **(c)**

Figure 19. Architecture #3 trajectory details showing altitude as a function of (a) time from launch to 6km altitude, (b) velocity from IAD deployment to 6 km, and (c) velocity from 200 m/s to parafoil deployment with Mach number contours.

Architecture #3, as shown in Figure 19, represents a mesospheric sample collection platform which utilizes a supersonic IAD and a precision guided parafoil to demonstrate more precise return of a suborbital sample retrieval system at moderate cost. The drag modulated downrange capability is enhanced by the maneuvering of a guided parafoil which is nominally deployed at 6 km altitude. The parafoil has the capability of reaching a specified target if deployed within 10 km radius of the target. Flight times of the parafoil are on the order of 20 minutes, thus giving a total system flight time of approximately 30 minutes. This architecture provides the greatest downrange control, capable of improving landed accuracies between 15 and 25 km, depending on the initial launch elevation angle. Sample retrieval can benefit from having a precise landing system by speeding up time to recovery on the ground.

This architecture combines precision guided parachute with extensive flight test experience with the relatively less technologically mature IAD.[31]

V. Conclusion

This investigation identified and evaluated several key system trades associated with capturing and returning mesospheric dust particles to the Earth's surface. Among the trade studies analyzed, primary focus was given to selection of the vehicle bus configuration along with assessing the performance and complexity of a range of deployable decelerators. For initial sample collection at velocities greater than 3 km/s, a thermal protection system is likely necessary to ensure payload survival. In order to obtain landing dispersions less than 40 km, the ideal initial sampling state should have a low velocity, high flight path angle and be delivered to as low of altitude as possible. By incorporating the launch vehicle into an end-to-end analysis, optimized trajectories for maximum time in the mesosphere, maximum range in the mesosphere, maximum number of particles captured in mesosphere, and maximum collected sample mass were obtained within given launch and payload mass constraints. Use of an IAD for downrange control was demonstrated and deployment conditions were characterized for a variety of vehicle parameters. For the optimized reference trajectory, downrange dispersions using drag modulation were shown to be reduced by approximately 6.8 km. Drag modulation control authority was shown to improve as payload mass increased and launch elevation angle decreased. Three reference architectures were derived from the reference trajectory in this study. Using a stock DGB decelerator system, architecture #1 provides a low complexity, high technology readiness level, option for sample recovery. Architecture #2 implements an IAD for sample recovery, *in lieu* of the limited deployment condition capable DGB. Implementation of a drag modulation algorithm coupled with an IAD, demonstrated downrange dispersion error reduction in architecture #3. The addition of a guided parafoil in architecture #3 further reduces the landed dispersion by an additional 10 km. The examined architectures provide differing levels of engineering complexity, cost, and capability to be examined in future studies.

Acknowledgments

The work presented was funded by the C.S. Draper Laboratory, Inc. under a University Research and Development project entitled "Deployable Decelerators for Small Atmospheric Recovery Missions." The authors would like to acknowledge Phil Hattis, Amer Fejzic, and Scott Thompson for their contributions to this investigation. The authors would also like to thank Jeremy Hill in the Space Systems Design Laboratory at Georgia Tech for contributions to the aerodynamics analysis presented in this work.

References

[1] Love, S.D., and Brownless, D.E., "A direct measurement of the terrestrial mass accretion rate of cosmic dust, Science, 262, 550-553, 1993.

[2] Mathews, J.D., et al., "The micro-meteoroid mass flux into the upper atmosphere Arecibo results and a comparison with prior estimates," *Geophys. Res. Lett*., 28 1929-1932, 2001.

[3] Turco, R.P., Toon, O.B., Whitten, R.C., Keesee, R.G., Hollenbach, D., 1982. Noctilucent clouds—simulation studies of their genesis, properties and global influences. Planetary and Space Science 30, 1147–1181.

[4] Goldberg, R. A., R. F. Pfaff, R. H. Holzworth, and F. J. Smith. "DROPPS: A Study of the Polar Summer Mesosphere with Rocket, Radar and Lidar." Geophysical Research Letters 28.8 (2001): 1407-410. Print.

[5] Stiller, G.P., Tsidu, G.M., von Clarmann, T., Glatthor, N., Hopfner, M., Kellmann, S., Linden, A., Ruhnke, R., Fischer, H., Lopez-Puertas, M., Funke, B., Gil-Lopez, S., 2005. "An enhanced HNO3 second maximum in the Antarctic midwinter upper stratosphere," 2003. Journal of Geophysical Research 110.

[6] Prather, M.J., Rodriguez, J.M., "Antarctic ozone: meteoric control of HNO3," Geophysical research letters [0094-8276] Prather yr:1988 vol:15 iss:1 pg:1

[7] Murphy, D.M., Thomson, D.S., Mahoney, M.J., "In Situ Measurements of Organizcs, Meteoritic Materials, Mercury, and Other Elements in Aerosols at 5 to 19 Kilometers," Science 282, 1664 (1998)

[8] Hawkes, R. L., S. C. Woodworth. "Do Some Meteorites Come from Intersellar Space?". RASC Journal. April 1997

[9] Soberman, R.K., "Extraterrestrial Dust Concentrations in the Upper Atmosphere," Smithsonian Contributions to Astrophysics, Vol. 11, p. 323, 1967.

[10] Saunders, R.W., and Plane, J.M.C., "A laboratory study of meteor smoke analogues: composition, optical properties and growth kinetics," J. Atmos. Sol.-Rerr. Phys., 68, 2182-2202, 2006.

[11] Soberman, R.K., Hemenway, C.L., Ryan, T.G., Chrest, S.A., Frissora, J., Fullham, E.F., "Micrometeorite Collection from a Recoverable Sounding Rocket I," Smithsonian Contributions to Astrophysics, Vol. 7, p.89.

[12] Blanchard, M.B., Farlow, N.H., "Contamination control during the design, fabrication, test, and launch of an upper atmospheric rocket payload," Contamination Control, V(5), 22-25. 1966.

[13]Ferry, G.V., Blanchard, M.B., Farlow, N.H., “Microparticle Collection Experiments during the 1966 Orionid and Leonid Meteor Showers,” *Journal of Geophysical Research*, Space Physics. Vol 75, No. 4, 1970.

[14]Hedin, J., J. Gumbel, and M. Rapp (2005), “The aerodynamics of smoke particle sampling,” in Proceedings of the 17th ESA Symposium on European Rocket and Balloon Programmes and Related Research, Sandefjord, Norway, Eur. Space Agency Spec. Publ., ESA SP-590,145–150.

[15]Goldberg, R.A., et al., (2001). The DROPPS program to study the polar summer mesosphere. *Greenhouse Gases, Aerosols and Dust*, 28(7). 1037-1046.

[16]Blix, T. A. and Thrane, E.: Noctilucent clouds and regions with polar mesopheric summer echoes studied by means of rocket-borne electron and ion DC-probes, *Geophys. Res. Lett*., 20, 2303–2306, 1993.

[17]Rodríguez, M.N., " Analysis of the dynamical behavior of the Minidusty rocket payloads, and its influence on the plasma probe measurements," MS Thesis. Department of Physics and Technology, University of Tromsø, Tromsø, Norway, 2007.

[18]Smiley, B., Rapp, M., Blix, T A., Robertson, S., Horanyi, M., Latteck, R., and Fiedler, J.: Charge and size distribution of mesospheric aerosol particles measured inside NLC and PMSE during MIDAS MaCWAVE 2002, *J. Atmos. Sol. Terr. Phys*., 68, 114–123, 2006.

[19]Gumbel, J., et al., The MAGIC campaign: An overview, Proc. 17th ESA Symposium on European Rocket and Balloon Programmes and Related Research (ESA SP-590), 139-144, 2005.

[20]Hedin, J., Gumbel, J., Waldemarsson, T., and Giovane, F.: The aerodynamics of the MAGIC meteoric smoke sampler, Advances in Space Research, 40, 818-824, 2007.

[21]Hedin, J., " Rocket-borne in-situ measurements in the middle atmosphere," PhD Thesis. Department of Meteorology, Stockholm University, Stockholm, Sweden, 2009.

[22]Soberman, R. K. et al., “ Techniques for rocket sampling of noctilucent cloud particles,” *Tellus*, 16, 1, Blackwell Publishing Ltd 2153-3490, 1964

[23]Farlow, N.H., Blanchard, M.B., Ferry, G.V., “Sampling with a Luster Sounding Rocket during a Leonid Meteor Shower,” *Journal of Geophysical Research, Space Physics*. Vol 71, No. 23, 1966.

[24]McIntyre, A., “AFCRL Space Science Research During 1967 (Annual Report to COSPAR),” Air Force Cambridge Research Labs L G Hanscom Field Mass, Technical report AD-665 853 Special repts. no. 70, 1 Jan-31 Dec 67.

[25]Strelnikova, I., et al., “Measurements of meteor smoke particles during the ECOMA-2006 campaign: 2. results,” *J. Atmos. Sol. Terr. Phys.*, 71, 486–496, 2009

[26]Brattli, A., el al., “The ECOMA 2007 campaign: rocket observations and numerical modelling of aerosol particle charging and plasma depletion in a PMSE/NLC layer,” *Ann. Geophys.*, 27, 2, 2009

[27]Abdu, M.A., et al., “ Aeronomy of the Earths Atmosphere and Ionosphere,” ISBN 978-94-007-0326-1

[28]Stober, G., et al., “The Geminid meteor shower during the ECOMA sounding rocket campaign: specular and head echo radar observations,” *Ann. Geophys*., 31, 3, 2013.

[29]Otero, R.E. and Braun, R.D.; "The Planetary Entry System Synthesis Tool: A Conceptual Design and Analysis Tool for EDL Systems," IEEEAC 1331, *2010 IEEE Aerospace Conference*, Big Sky, MT, March 2010.

[30]NASA Sounding Rocket Handbook, Goddard Spaceflight Center, Wallops Flight Facility, 2006

[31]Smith, B.P.; Tanner, C.L.; Mahzari, M.; Clark, I.G.; Braun, R.D.; and Cheatwood, F.M.; "A Historical Review of Inflatable Aerodynamic Decelerator Technology Development," IEEEAC 1276, *2010 IEEE Aerospace Conference*, Big Sky, MT, March 2010.

[32]Clark, I.; "Aerodynamic Design, Analysis and Validation of a Supersonic Inflatable Decelerator," Thesis. Department of Aerospace Engineering, Georgia Institute of Technology, Atlanta, GA, 2009.

[33]Davies, Carol, and Marla Arcadi. "Planetary Mission Entry Vehicles Quick Reference Guide. Version 3.0." NASA Technical Reports Server. NASA Ames Research Center, 30 July 2007. Web. 08 Jan. 2013.

[34]Burchell, M.J., et al., “Characteristics of cometary dust tracks in Stardust Aerogel and laboratory calibrations, Meteroirt. Planet. Sci., 43, 23-40, 2008

[35]Tanner, C.L.; Cruz, J.R.; and Braun, R.D.; "Structural Verification and Modeling of a Tension Cone Inflatable Aerodynamic Decelerator," AIAA 2010-2830, *51st AIAA/ASME/ASCE/AHS/ASC Structures, Structural Dynamics, and Materials Conference*, Orlando, FL, April 2010.

[36]Knacke, T. W. Parachute Recovery Systems: Design Manual. Santa Barbara, CA: Para Pub., 1992. Print.

[37]Hunten, D. M., R. P. Turco, and O. B. Toon. "Smoke and Dust Particles of Meteoric Origin in the Mesosphere and Stratosphere." *Journal of Atmospheric Sciences* 37 (1980): n. pag. Web.

[38]Lees, L., “Laminar Heat Transfer Over Blunt-Nosed Bodies at Hypersoinc Flight Speeds,” *Jet Propulsion*, vol. 26, no. 4, April. 1956, pp. 259-269, 274.

[39]Kinney, D. J., “Aero-Thermodynamics for Conceptual Design," AIAA 2004-13382*, 2004 AIAA Aerospace Sciences Meeting and Exhibit*, Reno, NV, Jan. 2004.

[40]McCoy, R.L., “MC Drag – A Computer Program for Estimating the Drag Coefficients of Projectiles,” US ARMY ARRADCOM TRR ARBRL – TR – 02293, February 1981.

[41]Munson B.R., Young, D.F., and Okiishi, T.H., 2002, Fundamentals of Fluid Mechanics, Fourth Edition, Wiley, New York.

[42]Sutton, K., Graves, R.A., Jr., “A General Stagnation-Point Convective-Heating Equation for Arbitrary Gas Mixtures, NASA TR R-376, 1971.

[43]Levy, L. L., “The Use of Drag Modulation to Limit the Rate at Which Deceleration Increases During Nonlifting Entry,” Tech. Rep. NASA TN D-1037, Ames Research Center,Washington, DC, Sept. 1961.

[44] Putnam, Z.R. and Braun, R.D.; "Precision Landing at Mars Using Discrete-event Drag Modulation," AAS-13-438, *23rd AAS/AIAA Spaceflight Mechanics Meeting*, Kauai, HI, February 2013.

[45] Silbert, M.N., Gilbertson, G.S., Moltedo, A.D., “High Altitude Decelerator Systems,” *AIAA 10th Aerodynamic Decelerator Conference*, April 1989, DOI: 10.2514/6.1989-882

[46] Silbert, M. N.. "Deployment of a spin parachute in the altitude region of 260,000 ft", *Journal of Spacecraft and Rockets*, Vol. 20, No. 1 (1983), pp. 11-14. DOI: 10.2514/3.28350

[47] Toohey, D., “Development of a Small Parafoil Vehicle for Precision Delivery,” M.S. Thesis, M.I.T., June 2005.

[48] Stara Technolgies Inc., Guided Parachute Systems, http://www.miniairdrop.com/MOSQUITO.html

[49] Justus, C.G., Leslie, F.W., “The NASA MSFC Earth Glocbel Reference Atmospheric Model – 2007 Version,” NASA TM-2008-215581, Nov 2008

[50] Smayda, M.G., Goyne, C.P., “Dispersion Reduction for a Sounding-Rocket Scramjet Flight Experiment,” *Journal of Spacecraft and Rockets*, Vol. 49, No. 3, Issue 3, pp 522-528

[51] Laub, B. and Venkatapathy, E., “Thermal Protection System Technology and Facility Needs for Demanding Future Planetary Missions," International Workshop on Planetary Probe Atmospheric Entry and Descent Trajectory Analysis and Science Proceedings, Lisbon, Portugal, Oct. 2003.